

# Using $Z \rightarrow \tau\tau$ events to calculate Tau ID scale factors using high $p_T$ Tau leptons

---

Diego Baron

Supervisor: Prof. Terence Wyatt

Examiner: Dr. Marco Gersabeck

University of Manchester  
Faculty of Science and Engineering  
School of Physics and Astronomy  
April, 2020

**Writing Period**

05. 07. 2016 – 05. 10. 2016

**Supervisor**

Prof. Terence Wyatt

**Examiner**

Dr. Marco Gersabeck

# Declaration

I hereby declare, that I am the sole author and composer of my thesis and that no other sources or learning aids, other than those listed, have been used. Furthermore, I declare that I have acknowledged the work of others by providing detailed references of said work.

I hereby also declare, that my Thesis has not been prepared for another examination or assignment, either wholly or excerpts thereof.

---

Place, Date

---

Signature



# **Abstract**

foo bar



# Contents

<b>1</b>	<b>Introduction</b>	<b>1</b>
<b>2</b>	<b>Tau physics overview</b>	<b>3</b>
2.1	The Tau Lepton . . . . .	3
2.2	Lepton Universality . . . . .	5
<b>3</b>	<b>Tau Reconstruction and Identification on ATLAS</b>	<b>9</b>
3.1	The LHC and the ATLAS experiment . . . . .	9
3.2	Tau Reconstruction and Identification on the ATLAS detector . . . . .	10
<b>4</b>	<b><math>Z \rightarrow \tau_{\text{had}}\tau_{\text{lep}}</math> tag and probe study</b>	<b>13</b>
4.1	Signal events . . . . .	13
4.2	Monte Carlo and Data Samples . . . . .	15
4.3	Event Selection . . . . .	16
4.4	Multi Jet Background Estimation . . . . .	17
<b>5</b>	<b>Results</b>	<b>19</b>
5.1	$\mu\tau$ Final state . . . . .	19
5.2	$e\tau$ Final state . . . . .	19
5.3	Monte Carlo and data discrepancies . . . . .	19
<b>6</b>	<b>Conclusions and prospects</b>	<b>21</b>
	<b>Bibliography</b>	<b>24</b>



# List of Figures

1	Tau leptonic decay mode. Tau lepton is kinematically allowed to decay into muons or electrons, not that in this decay mode two neutrinos of different flavour are produced. . . . .	4
2	Tau hadronic decay mode. Tau lepton is kinematically allowed only to decay into hadrons containing up, down and strange quarks. This results on final states containing multiple pions or kaons [1]. . . . .	4
3	Combined results from BABAR,Belle and LHCb with $1-\sigma$ contour. The average calculated by the Heavy Flavour Averaging Group [2] is compared with the SM predictions. . . . .	7
4	Graphic representation that shows the main differences between a 3-prong $\tau_{\text{had}}$ and a jet originated from quark or gluon radiation (QCD jets). Charged hadrons are shown as thick lines and dashed lines represent neutral particles. The green cone is drawn to depict how $\tau_{\text{had}}$ product decays are more collimated. . . . .	11
5	Comparisson between the performance of BDT and RNN algorithms. Working points are shown as points. Notice there is a trade off between true $\tau_{\text{had}}$ efficiency and background rejection power. Taken from [3]. . . . .	11
6	Distribution of the RNN scores for true and fake $\tau_{\text{had}}$ candidates for 1-prong (a) and 3-prong (b) cases. Taken from [3]. . . . .	12
7	The two different types of topologies that define signal events. On the right, when the missing energy is between the visible objects two neutrinos are assumed to be responsible for all the missing energy. On the left, only one neutrino is assumed to be flying on the direction of the visible object closest to the missing energy. . . . .	14
8	Graphical representation of the different values of $\Omega$ depending on the region where the $\cancel{E}_T$ is located in the event. . . . .	15
9	Distribution of $\Omega$ for $Z \rightarrow \tau_{\text{had}}\mu$ final state. . . . .	17
10	$m_{\text{reco}}$ distribution for the in between region (a) and the outside region (b). . . . .	17
11	Distribution of the variables used for rejecting $\tau_{\text{had}}$ fakes coming from electrons. On the right $m(e, \tau_{\text{had}})$ distribution (a) and on the left the eBDTScore distribution (b). . . . .	17
12	$p_T(\tau_{\text{had}})$ distribution for the in between (a) and outside (b) regions. . . . .	18
13	Caption that appears in the figlist . . . . .	22



# List of Tables

1	Tau hadronic decay modes branching fractions. . . . .	5
2	Working points with their corresponding true $\tau_{\text{had}}$ selection efficiency and the background rejection factors. The scores are shown for both RNN and BDT algorithms. . . . .	11
3	List of MC event generators used. . . . .	16
4	Table caption . . . . .	21



# List of Algorithms



# 1 Introduction



## 2 Tau physics overview

This chapter is a review of the Tau lepton properties. They include the nature of this particle, its interactions with other the Standard Model (SM) particles, its main decay modes and the physics implications of the so called Lepton Universality (LU), one of the SM predictions.

### 2.1 The Tau Lepton

The Tau is a spin- $\frac{1}{2}$ , electrically charged particle that belongs to the same family of particles as the electron, the muon and the neutrinos, they are all called *leptons*. Leptons are elementary particles that interact only via the weak and electromagnetic interactions, for the latter case only if they have electric charge.

The first hints for the tau existence came from experiments conducted at the Stanford Linear Accelerator Center and Lawrence Berkeley National Laboratory [4]. They discovered 64 events of the form:

$$e^+ + e^- \rightarrow e^\pm + \mu^\mp + \geq 2 \text{ undetected particles}, \quad (1)$$

for which there was no conventional explanation at the time. Later on, it was discovered that these events came from the production of a pair of new particles, two taus that subsequently decayed onto one electron, a muon and four neutrinos. Events like,

$$e^+ + e^- \rightarrow \tau^+ \tau^- \rightarrow e^\pm + \mu^\mp + 4\nu, \quad (2)$$

were later explored to derive tau mass and spin, confirming the existence of a third generation of leptons.

The tau mass being  $1776.86 \pm 0.12$  MeV allows this lepton not only to decay into the other lighter lepton generations (*leptonic tau decays*), as its shown on Fig.1 , but into *hadrons*. These are particles made of quarks, all the decay channels of the tau containing hadrons in the final state are called *hadronic tau decays*. An example of this decay mode is shown in Fig.2 Naively, if we were to estimate the branching fraction for hadronic and leptonic tau decay modes, defined as:

$$\beta(\tau \rightarrow X \nu_\tau) = \frac{\Gamma(\tau \rightarrow X \nu_\tau)}{\Gamma_{\text{tot}}}, \quad (3)$$

where X could be any group of leptons or hadrons and  $\Gamma_{\text{tot}}$  is the total decay width for the tau, we could argue that the contribution from the hadronic decays triples the contribution for one of

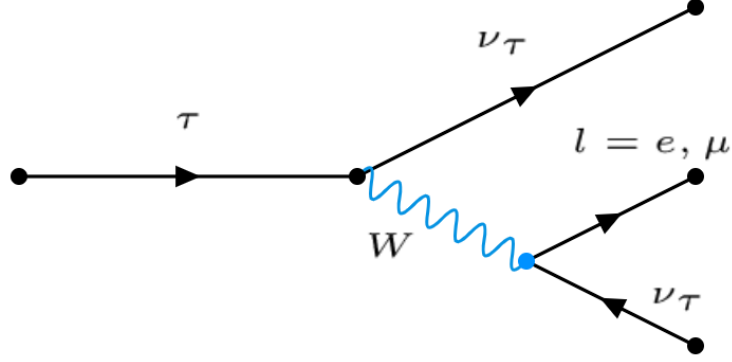


**Figure 1:** Tau leptonic decay mode. Tau lepton is kinematically allowed to decay into muons or electrons, not that in this decay mode two neutrinos of different flavour are produced.

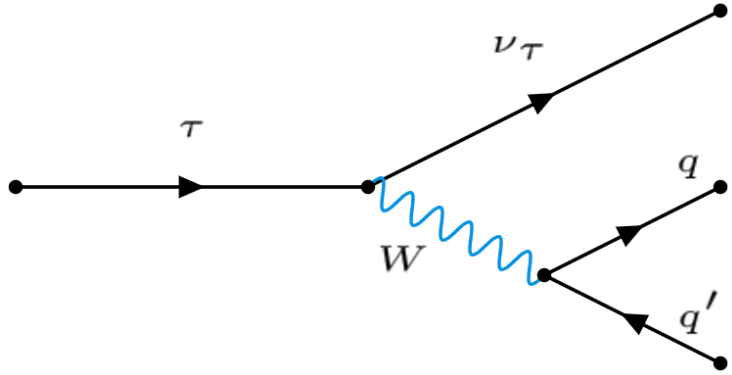


**Figure 2:** Tau hadronic decay mode. Tau lepton is kinematically allowed only to decay into hadrons containing up, down and strange quarks. This results on final states containing multiple pions or kaons [1].

the leptonic modes. This is because in any hadronic decay, we would have to count 3 different diagrams, like the one in Fig.2 because of the 3 colour possibility for the quarks.

Thus,

$$\beta(\tau \rightarrow l\nu_l\nu_\tau) \approx 20\% \quad l = e, \mu; \quad (4)$$

$$\beta(\tau \rightarrow X\nu_\tau) \approx 60\% \quad X = \text{hadrons+neutrinos}. \quad (5)$$

In fact, this naive estimation is not so bad. Actual values for the leptonic branching ratios are [5]:

$$\beta(\tau \rightarrow e\nu_e\nu_\tau) = 17.82 \pm 0.04\% \quad (6)$$

$$\beta(\tau \rightarrow \mu\nu_\mu\nu_\tau) = 17.39 \pm 0.04\%, \quad (7)$$

and the small difference is due to the mass variation between the muon and the electron.

On the other hand, the hadronic decays of the tau are more varied and can contain much more particles in the final states. The vast majority of hadronic tau decays have charged or neutral

Decay mode	Branching fraction
$\pi^\pm \nu_\tau$	11.1 %
$\pi^\pm \pi^0 \nu_\tau$	25.4%
$\pi^\pm \geq 2\pi^0 \nu_\tau$	9.1%
$3\pi^\pm \nu_\tau$	9.1%
$3\pi^\pm \geq 1\pi^0 \nu_\tau$	4.6%
others	5.5%

**Table 1:** Tau hadronic decay modes branching fractions.

pions in the final states, but more exotic decays including kaons also happen. Branching ratios for the most important tau hadronic decays are showed in Table 1.

## 2.2 Lepton Universality

The SM predicts that all charged leptons ( $e, \mu, \tau$ ) interact via the electromagnetic and weak forces and explains that this interactions can be seen as the interchange of *vector bosons*, the photon ( $\gamma$ ) and the W and Z bosons respectively. Specifically, in the SM the form of the interaction does not depend on the lepton generation. This feature of the SM is called *lepton universality* and it can be understand as that many physical process for electrons, muons and taus are almost identical copies of each other (although some small discrepancies arise from the fact that lepton masses are different and extictly speaking lepton universality is not a exact symmetry).

For instance, tau leptonic decay widths are an outstanding way to test lepton universality hypothesis. If we start considering muon decay, at low energy we can consider this process to be a point like interaction well described by Fermi theory [6]. In this case, if we approximate the electron and neutrinos as being massless particles, a dimensionally correct expression for the width will be of the form:

$$\Gamma(\mu \rightarrow e + \nu_e + \nu_\mu) = K G_F^2 m_\mu^5, \quad (8)$$

where  $G_F = 1.1666 \times 10^{-5} \text{ GeV}^{-2}$  is the Fermi coupling constant and  $K$  is a constant that depends on the form of the interaction. If we assume lepton universality holds, the respective widths for the leptonic tau decay modes, will have the form:

$$\Gamma(\tau \rightarrow e + \nu_e + \nu_\tau) = K G_F^2 m_\tau^5 \quad (9)$$

$$\Gamma(\tau \rightarrow \mu + \nu_\mu + \nu_\tau) = \Gamma(\tau \rightarrow e + \nu_e + \nu_\tau), \quad (10)$$

and this explains why to a good approximation leptonic branching fractions for tau decay are equal. Moreover, we can obtain a relation between tau and muon lifetimes. We know that,

$$\tau_l = \frac{1}{\Gamma_{\text{Tot}}} = \frac{\beta(l \rightarrow e\nu_e\nu_l)}{\Gamma(l \rightarrow e\nu_e\nu_l)}, \quad (11)$$

also that  $\beta(\mu \rightarrow e\nu_e\nu_\mu) = 1$  and taking into account eq.(6) we can take the ratio between eq.(11)

for  $l = \tau, \mu$  to obtain:

$$\frac{\tau_\tau}{\tau_\mu} = \frac{\beta(\tau \rightarrow e\nu_e\nu_\tau)}{\beta(\mu \rightarrow e\nu_e\nu_\mu)} \left( \frac{m_\mu}{m_\tau} \right)^5 = (1.328 \pm 0.004) \times 10^{-7}. \quad (12)$$

This is consistent with the experimental lifetimes ratio  $(1.3227 \pm 0.0005) \times 10^{-7}$ . This agreement on lifetimes that differ on 7 orders of magnitude is a good proof that lepton universality holds on W decays at the tau mass scale.

Very precise test of LU have been done by  $e^-e^+$  colliders (LEP1, SLC and LEP2). Measurements of the ratios between the leptonic decay widths of the Z boson have been performed and are consistent with the SM [7]:

$$\frac{\Gamma(Z \rightarrow \mu^+\mu^-)}{\Gamma(Z \rightarrow e^+e^-)} = 1.0009 \pm 0.0028, \quad (13)$$

$$\frac{\Gamma(Z \rightarrow \tau^+\tau^-)}{\Gamma(Z \rightarrow e^+e^-)} = 1.0019 \pm 0.0032. \quad (14)$$

LU has also been tested in W boson decays, a combination of measurements made by different experiments of the branching fractions between the first two families of leptons are consistent with SM predictions [8]:

$$\frac{\beta(W^- \rightarrow e^-\bar{\nu}_e)}{\beta(W^- \rightarrow \mu^-\bar{\nu}_\mu)} = 1.004 \pm 0.008. \quad (15)$$

But measurements including the third lepton family, apart from being less precise due to the more challenging reconstruction of the  $\tau$  lepton final states are in tension with SM [9]:

$$\frac{\Gamma(W^- \rightarrow \tau^-\bar{\nu}_\tau)}{\Gamma(W^- \rightarrow e^-\bar{\nu}_e)} = 1.063 \pm 0.027, \quad (16)$$

$$\frac{\Gamma(W^- \rightarrow \tau^-\bar{\nu}_\tau)}{\Gamma(W^- \rightarrow \mu^-\bar{\nu}_\mu)} = 1.070 \pm 0.026. \quad (17)$$

This results show that LU between the two first lepton family holds with a precision of 0.3% and 0.8% in Z and W decays respectively. Constraints between the third and the other two generations of leptons are of similar precision on Z boson decays (0.3%), but then times worse for W boson decays (3%) and somewhat in tension with SM prediction. An example of this is a measurement exhibiting a tension of  $2.6\sigma$  from the SM expectation [9]:

$$\frac{2\Gamma(W^- \rightarrow \tau^-\bar{\nu}_\tau)}{\Gamma(W^- \rightarrow e^-\bar{\nu}_e) + \Gamma(W^- \rightarrow \mu^-\bar{\nu}_\mu)} = 1.066 \pm 0.025. \quad (18)$$

Furthermore, measurements from LHCb, BaBar and Belle experiments have shown consistent deviations from the SM predictions [10]. These experiments have independently measured a deviation

on  $\bar{B}$  meson semi-leptonic branching ratios, specifically:

$$R_D = \frac{\beta(\bar{B} \rightarrow D\tau^-\bar{\nu}_\tau)}{\beta(\bar{B} \rightarrow De^-\bar{\nu}_e)} \quad (19)$$

$$R_{D^*} = \frac{\beta(\bar{B} \rightarrow D^*\tau^-\bar{\nu}_\tau)}{\beta(\bar{B} \rightarrow D^*e^-\bar{\nu}_e)}. \quad (20)$$

The combined results for the different experiments are shown in Fig.3 . These measurements represent a  $3.08\sigma$  deviation from the SM predictions, but even though they represent a hint of new physics, these results also have to be taken with care since at this point it could be that systematic uncertainties are being underestimated or statistical deviations are larger than expected. In this matters, future analysis from experiments like LHCb and Belle with larger available datasets will be very important to untangle this situation.

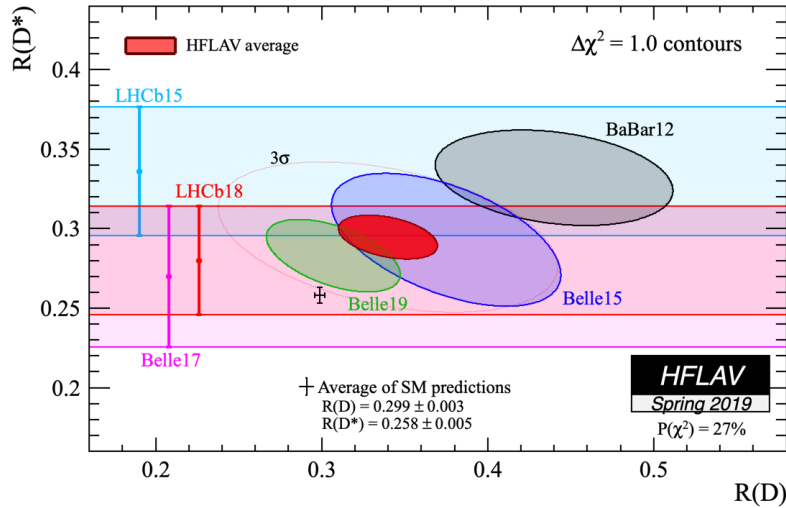


**Figure 3:** Combined results from BABAR,Belle and LHCb with  $1-\sigma$  contour. The average calculated by the Heavy Flavour Averaging Group [2] is compared with the SM predictions.



# 3 Tau Reconstruction and Identification on ATLAS

In this chapter, a review of the ATLAS detector at the Large Hadron Collider and a description of the reconstruction and identification of hadronic Tau decays on ATLAS are presented.

## 3.1 The LHC and the ATLAS experiment

The Large Hadron Collider (LHC) is the largest particle accelerator currently operated by the European Organization for Nuclear Research (CERN). The LHC uses a 27 km tunnel where 2090, 15 m long, dipolar superconducting magnets bend the trajectories of two proton beams going in opposite directions. Each of the magnets is capable of producing a 8,33 T magnetic field and thus bending protons with an energy up to 7 TeV. The magnets are cooled down to 1.9 K in order to reach the superconducting state and the vacuum inside the tubes is of the order of  $10^{-9}$  mbar. During Run II, proton beams were accelerated to an energy of 6.5 TeV and they are collided in 4 interaction points where the detector experiments are located.

One of these experiments is the ATLAS (A Toroidal LHC ApparatuS) detector. It is a multi-purpose particle detector, capable of discovering new physics but also perform high precision SM measurements, a complete description of the ATLAS design can be found at [11]. ATLAS is a cylindrical detector composed by sub-detectors arranged in shells. The most inner layers are surrounded by a superconducting solenoid that generates a 2 T solenoidal magnetic field. ATLAS uses a right-handed coordinate system with its origin at the interaction point (IP) in the centre of the detector, the z-axis points along the beam pipe. The x-axis points towards the centre of the LHC ring and the y-axis along the azimuth direction. The angle  $\phi$  is defined in the  $x - y$  plane and pseudorapidity is defined in terms of the polar angle  $\theta$  as  $\eta = -\log \tan(\theta/2)$ . The angular distance is measured in units of  $\Delta R \equiv \sqrt{(\Delta\phi)^2 + (\Delta\eta)^2}$ .

The most inner detector is in charge of vertex reconstruction and it consist of a silicon pixel, silicon microstrip and transition radiation tracking detectors. The system has a coverage of  $|\eta| < 2.5$ . The tracker system is followed by a lead/liquid-argon electromagnetic calorimeter (EC) and a steel/scintillator-tile hadron calorimeter (HC) that provide energy measurements with high granularity for electromagnetic showers and hadrons. The end-cap and forward EC and HC use LAr technology detectors and extend up to a  $|\eta| = 4.9$  region. The outermost detection system is a muon spectrometer that takes advantage of the bending power of a system of three air-core toroidal superconducting magnets.

## 3.2 Tau Reconstruction and Identification on the ATLAS detector

Leptonically decaying taus ( $\tau_{\text{lep}}$ ), may have a higher impact parameter and tend to have a softer  $p_T$  spectrum compared with prompt W or Z boson decays to muons or electrons. These variables are not sufficient in principle to differentiate between  $\tau_{\text{lep}}$  and prompt muons or electrons. In the case of hadronically decaying taus ( $\tau_{\text{had}}$ ), as we will see, there are a lot more variables we could use to tag the presence of a  $\tau_{\text{had}}$ .

As we saw in section 2.1,  $\tau_{\text{had}}$  decays can be classified in 1-prong or 3-prong, depending on the number of charged particles in the decay. A detailed review of the reconstruction procedure is discussed on [12].  $\tau_{\text{had}}$  candidates are seeded by jets using the anti- $k_t$  algorithm [13], with a distance parameter of 0.4. Jets are required to have  $p_T > 10$  GeV and  $|\eta| < 2.5$ . Candidates between the barrel and forward calorimeter ( $1.37 < |\eta| < 1.52$ ) are excluded due to poor instrumentation in this region.

The axis of the seed jet is defined by the energy-weighted barycentre of all clusters of calorimeter cells, called *TopoClusters* [14]. The  $\tau_{\text{had}}$  vertex is defined as the vertex with the highest  $p_T$ -weighted fraction of all tracks with  $p_T > 0.5$  GeV within a cone of  $R = 0.2$  around the seed jet axis. Tracks within a cone of  $R = 0.4$  are classified with a set of boosted decision trees (BDTs) into core and isolation tracks, the number of core tracks defines the number of prongs. Candidates with neither one or three tracks are rejected. Additionally, the sum of the charge of the tracks is required to be  $\pm 1$ .

The tau reconstruction algorithm does not provide discrimination against jets that could mimic the signal of a  $\tau_{\text{had}}$  decay in the detector. Therefore, algorithms that perform this task have been developed. Previously, a BDT was used to discriminate jets against  $\tau_{\text{had}}$ . Recently, a recurrent neural network (RNN) classifier that provides improved performance than the BDTs is in use [3].

The RNN makes use of a set of variables like:  $\tau_{\text{had}}$  track features, information about energy deposits on the calorimeters clusters and high level features like the mass of the  $\tau_{\text{had}}$  candidate tracks. These variables are used to exploit the differences in the shapes of the showers between  $\tau_{\text{had}}$  and jets. In general,  $\tau_{\text{had}}$  showers tend to be more collimated and to have fewer tracks than jets. A representation of this is shown in Fig.4.

Separated algorithms are trained for 1-prong and 3-prongs. The final RNN score assigned to each event corresponds to the fraction of rejected true  $\tau_{\text{had}}$ , independent of  $p_T$  and number of interaction per bunch crossing (pileup). Four working points with increasing background rejection are defined to be used in physics analysis. The working points and background rejection factors are shown in Table 2. A plot comparing the true  $\tau_{\text{had}}$  selection efficiency versus the background rejection power for the RNN and BDT algorithm is shown in Fig.5 , the performance of the RNN is better than the BDT classifier. Finally, the distribution for the RNN score for true and fake  $\tau_{\text{had}}$  is shown in Fig. , for both 1-prong and 3-prong decays.

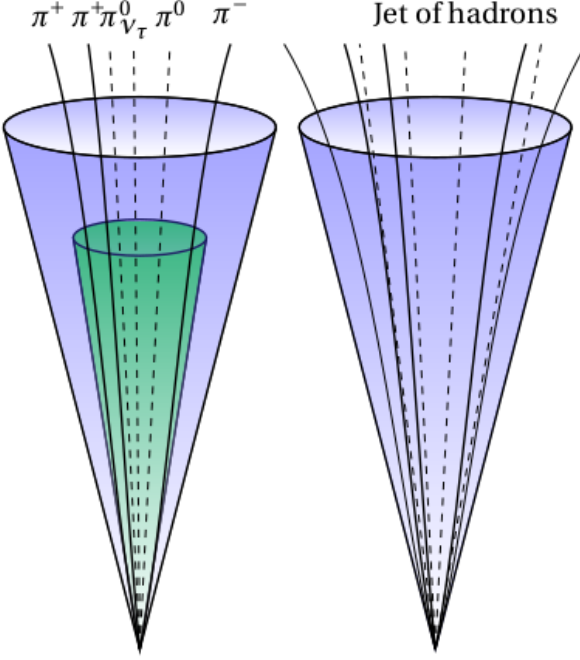


**Figure 4:** Graphic representation that shows the main differences between a 3-prong  $\tau_{\text{had}}$  and a jet originated from quark or gluon radiation (QCD jets). Charged hadrons are shown as thick lines and dashed lines represent neutral particles. The green cone is drawn to depict how  $\tau_{\text{had}}$  product decays are more collimated.

Working point	Singal efficiency (%)		BG rejection BDT		BG rejection RNN	
	1-prong	3-prong	1-prong	3-prong	1-prong	3-prong
Tight	60	45	40	400	70	700
Medium	75	60	20	150	35	240
Loose	85	75	12	61	21	90
Very loose	95	95	5.3	11.2	9.9	16

**Table 2:** Working points with their corresponding true  $\tau_{\text{had}}$  selection efficiency and the background rejection factors. The scores are shown for both RNN and BDT algorithms.

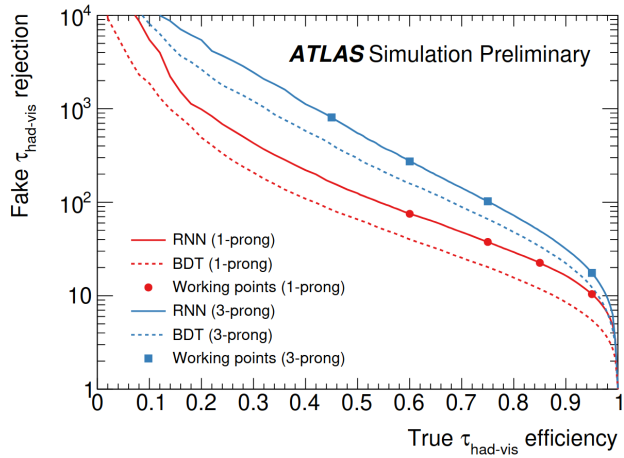


**Figure 5:** Comparisson between the performance of BDT and RNN algorithms. Working points are shown as points. Notice there is a trade off between true  $\tau_{\text{had}}$  efficiency and background rejection power. Taken from [3].

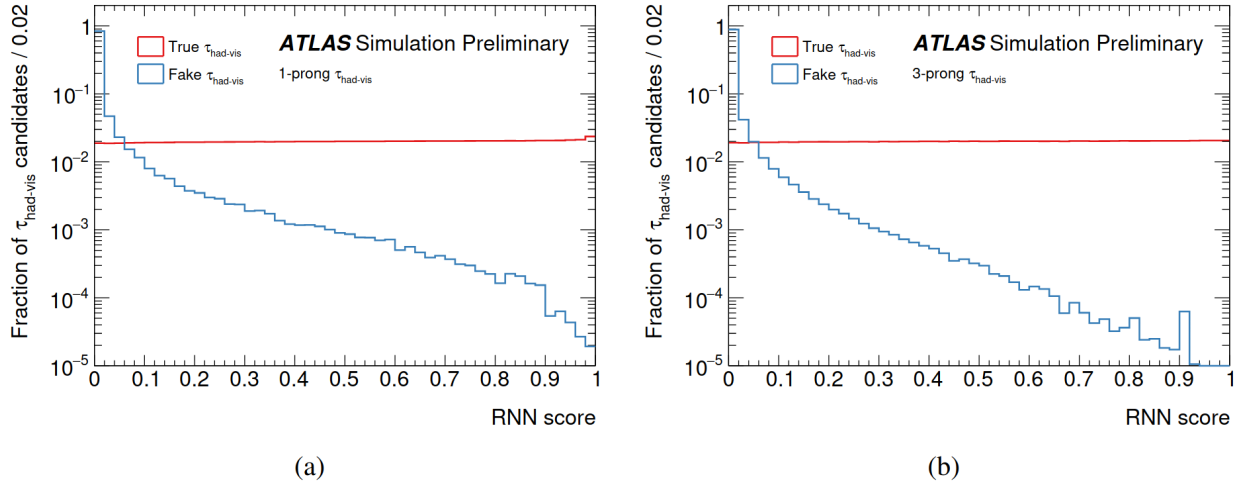


**Figure 6:** Distribution of the RNN scores for true and fake  $\tau_{\text{had}}$  candidates for 1-prong (a) and 3-prong (b) cases. Taken from [3].

## 4 $Z \rightarrow \tau_{\text{had}}\tau_{\text{lep}}$ tag and probe study

This chapter describes the analysis methodology of using  $Z \rightarrow \tau\tau$  events to measure Monte Carlo correction factors for tau identification algorithms on the high- $p_T$  region.

As we saw in the previous section different working points are defined for RNN score relative to the efficiency of selecting true  $\tau_{\text{had}}$  candidates. When the efficiency of the working points is measured in data and simulation, a correction factor is derived and then applied to the simulation in order for the signal efficiency to agree between data and simulation REF TAU ID PERFORMANCE. Because of the top quark mass,  $t\bar{t}$  events are used as a source of high momentum taus for measuring correction factors on the high- $p_T$  bins. But as we already saw in section 2.2, LU may not hold on W decays. For that reason our study is aimed to use  $Z \rightarrow \tau\tau$  events for deriving simulation correction factors on the high- $p_T$  region.

### 4.1 Signal events

The type of  $Z \rightarrow \tau\tau$  events we consider as signal are when one the taus decays hadronically and the other leptonically, either into an electron or a muon ( $Z \rightarrow \tau\tau \rightarrow \tau_h + l = \mu, e$ ). Thus, our final states will include a  $\tau_{\text{had}}$  candidate and a lepton  $l = e, \mu$ . The presence of this lepton will be used as our tag. Generally, in  $Z \rightarrow \tau\tau$  events, the taus are produced back to back and their  $p_T$  spectrum does not go very high. One way to select events where the taus are boosted on the transverse plain is to look for events where the opening angle in the transverse plane between the taus ( $\Delta\phi(\tau_{\text{had}}, \tau_{\text{lep}})$ ) is more acute. For these events, the missing transverse momentum ( $\cancel{E}_T$ ) is assumed to come from the neutrinos produced in the decays of the tau leptons. Due to the fact that two neutrinos are produced in the leptonic decay mode we expect our events to have a larger  $\cancel{E}_T$  component along the  $\tau_{\text{lep}}$  direction.

We classify our events in two types of topologies. First, events where the  $\cancel{E}_T$  is inside the opening angle between the visible objects, in this kind of events we assume the missing energy is due to a pair of neutrinos flying in the same direction as the visible objects. This is shown in Fig.7a . In this case, we solve the following equation to obtain the momentum of the neutrinos:

$$\vec{p}_{T_{\nu_l}} + \vec{p}_{\nu_h} = \vec{p}_{T_{\text{miss}}}, \quad (21)$$

given the following set of constraints (*collinear approximation*):

$$\phi(\nu_l) = \phi(l), \quad (22)$$

$$\phi(\nu_h) = \phi(\tau_{\text{had}}), \quad (23)$$

$$\eta(\nu_l) = \eta(l), \quad (24)$$

$$\eta(\nu_h) = \eta(\tau_{\text{had}}). \quad (25)$$

The second case is when the  $\not{E}_T$  is outside the angle formed by the visible objects, as is shown in Fig.7b, in this case the assumption is that only one neutrino is responsible for the majority of the  $\not{E}_T$ , a neutrino flying in the direction of the visible object that is closest to the  $\not{E}_T$ . We use the following equations to obtain the neutrino momentum:

$$p_{T\nu} = \not{E}_T \cos(\Delta\phi(\tau_{\text{closer}}, \not{E}_T)), \quad (26)$$

$$\phi(\nu) = \phi(\tau_{\text{closer}}), \quad (27)$$

$$\eta(\nu) = \eta(\tau_{\text{closer}}), \quad (28)$$

where  $\tau_{\text{closer}}$  stands for the visible object closest to the direction of the missing energy.

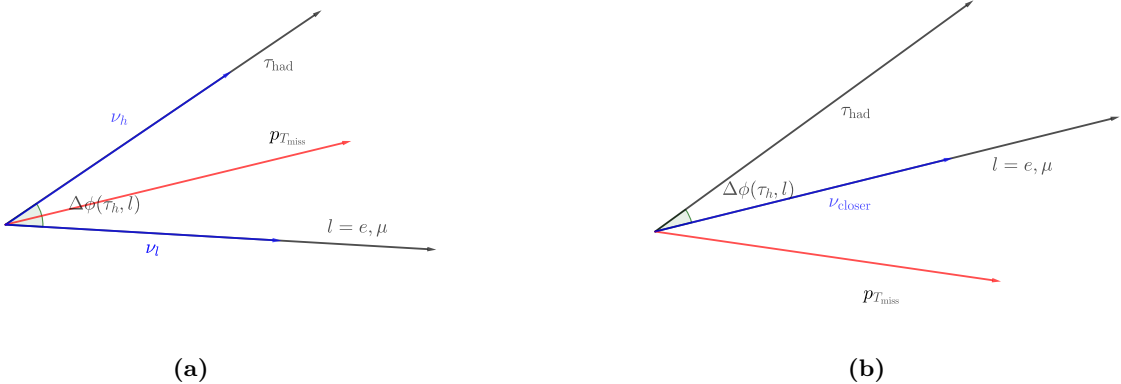


**Figure 7:** The two different types of topologies that define signal events. On the right, when the missing energy is between the visible objects two neutrinos are assumed to be responsible for all the missing energy. On the left, only one neutrino is assumed to be flying on the direction of the visible object closest to the missing energy.

We define a variable called  $\Omega$  in order to classify our events in the different topologies already described. First we define:

$$\omega = \frac{\Delta\phi(\tau_{\text{close}}, \not{E}_T)}{\Delta\phi(\tau_{\text{had}}, \tau_{\text{lep}})}, \quad (29)$$

then,

- when  $\not{E}_T$  is inside the opening angle between the visible objects but closer to  $\tau_{\text{had}}$ :

$$\Omega = \omega, \quad (30)$$

- when  $\cancel{E}_T$  is still inside, but closer to  $\tau_{\text{lep}}$ :

$$\Omega = 1 - \omega. \quad (31)$$

- If  $\cancel{E}_T$  is outside and closer to  $\tau_{\text{had}}$ :

$$\Omega = -\omega, \quad (32)$$

- and finally, if  $\cancel{E}_T$  is outside and closer to  $\tau_{\text{lep}}$ :

$$\Omega = \omega + 1. \quad (33)$$

Thus,  $\Omega$  is a continuous variable that give us information on the topology of the event. When  $\cancel{E}_T$  is inside the visible system it has values in the interval  $[0,1]$ . Exactly 0 when  $\cancel{E}_T$  is in the  $\tau_{\text{had}}$  direction and 1 when is on the  $\tau_{\text{lep}}$  direction.  $\Omega$  has negative values when  $\cancel{E}_T$  is outside and closer to the  $\tau_{\text{had}}$  candidate and has positive and values greater than 1 when is outside and closer to the  $\tau_{\text{lep}}$ . A diagram describing the  $\Omega$  values is shown in Fig.8. As we will see later the event

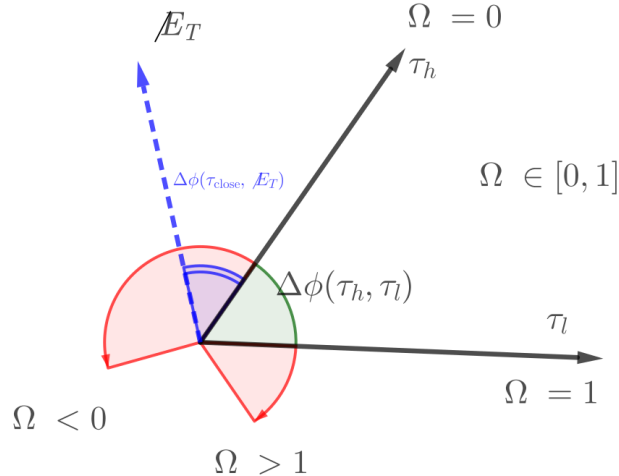


**Figure 8:** Graphical representation of the different values of  $\Omega$  depending on the region where the  $\cancel{E}_T$  is located in the event.

classification into this two different type of topologies will allow us to reconstruct and exploit kinematical variables as the invariant mass of the di-tau system, the Z boson transverse momentum ( $Z_{p_T}$ ) and the angular distribution of the objects in the event.

## 4.2 Monte Carlo and Data Samples

The data used for this study has been recorded during the Run-II of the LHC. This corresponds to the 2015-2018 data taking period, the total integrated luminosity corresponds to  $139.2 \text{ fb}^{-1}$  of proton-proton collisions at a centre-of-mass energy of  $\sqrt{s} = 13 \text{ TeV}$ .

Process	Event Generator
$Z \rightarrow \tau\tau$	Powheg+Pythia8 and Sherpa
$Z \rightarrow ee$	Powheg+Pythia8
$Z \rightarrow \mu\mu$	Powheg+Pythia8
$W \rightarrow l\nu_l$	Powheg+Pythia8
$t\bar{t}$	Powheg+Pythia8
Single $t$	Powheg+Pythia8
Diboson	Powheg+Pythia8

**Table 3:** List of MC event generators used.

Monte Carlo (MC) samples are used for signal and background simulation. For  $Z \rightarrow \tau\tau$  events two MC samples are used, Powheg+Pythia8 and Sherpa. For the rest of the samples Powheg+Pythia8 is used. Table 3 shows the MC generators used for each process.

### 4.3 Event Selection

The basic selection for our  $Z \rightarrow \tau_{\text{had}}\tau_{\text{lep}}$  includes events with exactly one  $\tau_{\text{had}}$  candidate and one lepton, a muon or an electron. The  $\tau_{\text{had}}$  and lepton pair need to have opposite charge. As we said, the presence of the lepton will be used as our tag, thus, a lepton trigger is required to be fired with an online requirement on the  $p_T(\mu) \geq 20$  ( $p_T(e) \geq 24$ ) GeV for 2015 data taking period. For 2016-2018 the requirement is  $p_T(\mu, e) \geq 26$  GeV. The muons are required to pass a *medium* ID requirement and the electron has to pass a *tight* ID filter. Additionally, both muons and electrons have to pass an offline  $p_T$  requirement to be greater than 27 GeV. Finally, the opening angle between the two visible objects  $\Delta\phi(\tau_{\text{had}}, l) \leq 2\pi/3$ .

Events containing b jets are vetoed in order to reject  $t\bar{t}$  events. Also an isolation criteria is required to be passed by the leptons: for the muon (electron), the scalar sum of the  $p_T$  of the tracks within a cone of  $\Delta R = 0.3(0.2)$  of the muon (electron) must be less than 0.06 times the muon (electron)  $p_T$ . Additionally for the electron, the sum of the calorimeter cluster energy in a cone of size  $\Delta R = 0.2$  must be 0.06 times the electron  $p_T$ . Then, as we said in section 4.1, we expect signal events to peak around  $\Omega = 1$ , thus we select events where  $\Omega \in (0, 1.4)$ . Fig.9 shows the  $\Omega$  distribution for  $Z \rightarrow \tau_{\text{had}}\mu$  final state. Additionally, a cut on the reconstructed invariant mass ( $m_{\text{reco}}$ ) of the event is made, the cut aims to pick events where the invariant mass is around the Z boson mass ( $70 \leq m_{\text{reco}} \leq 110$  GeV). The invariant mass of the final states is calculated depending on the event topology. For events where  $\Omega \in [0, 1]$  (*in between events*),  $m_{\text{reco}}^2 = (q_l + q_{\tau_{\text{had}}} + q_{\nu_l} + q_{\nu_{\tau_{\text{had}}}})^2$  and when the  $\cancel{E}_T$  is outside (*outside events*),  $(m_{\text{reco}} - 5)^2 = (q_l + q_{\tau_{\text{had}}} + q_{\nu})^2$ . In the latter case we manually add 5 GeV to maintain our cuts consistent, since in this region the Z mass is underestimated. Fig. shows the distribution of  $m_{\text{reco}}$  for the in between and outside  $Z \rightarrow \tau_{\text{had}}\mu$  events.

In addition, for the  $Z \rightarrow \tau_{\text{had}}e$  final state, we add two cuts aimed to reject events where the  $\tau_{\text{had}}$  candidate is faked by an electron. First to reject  $Z \rightarrow ee$  events, a requirement on the invariant mass of the electron and  $\tau_{\text{had}}$  candidate is made,  $m(e, \tau_{\text{had}}) < 80$  GeV. Then, we also make use

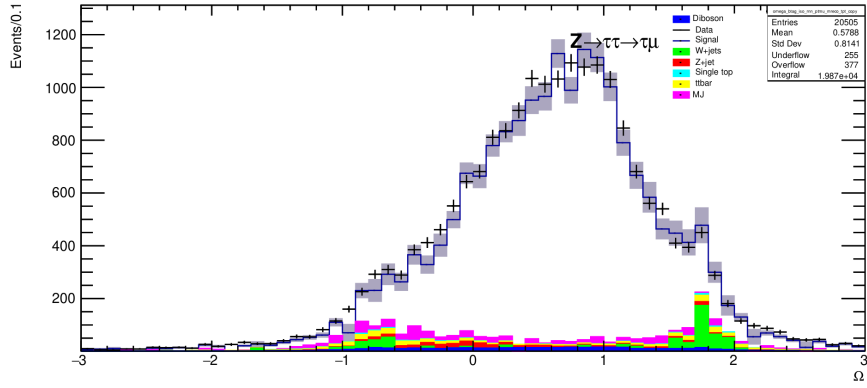


**Figure 9:** Distribution of  $\Omega$  for  $Z \rightarrow \tau_{\text{had}}\mu$  final state.

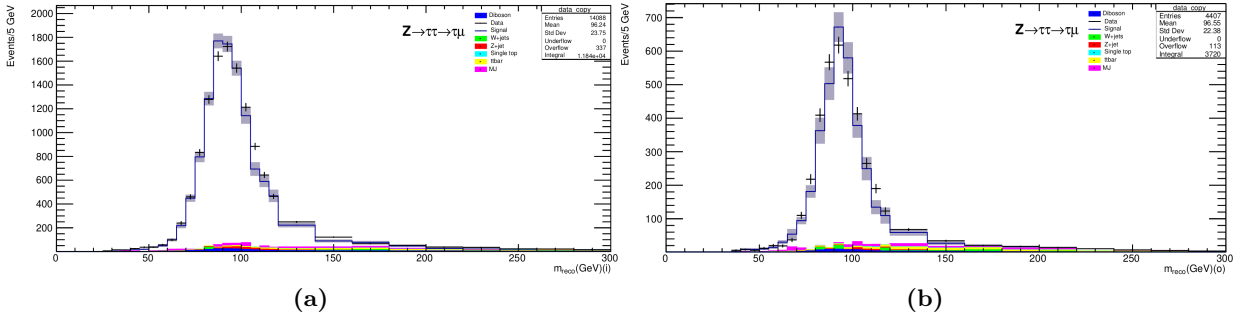


**Figure 10:**  $m_{\text{reco}}$  distribution for the in between region (a) and the outside region (b).

of an ID algorithm to discriminate electrons from real  $\tau_{\text{had}}$ . In our case,  $\text{eBDTScore} \geq 0.06$ . The distributions for this variables are shown in Fig.11. Finally, in order to measure the tau ID scale

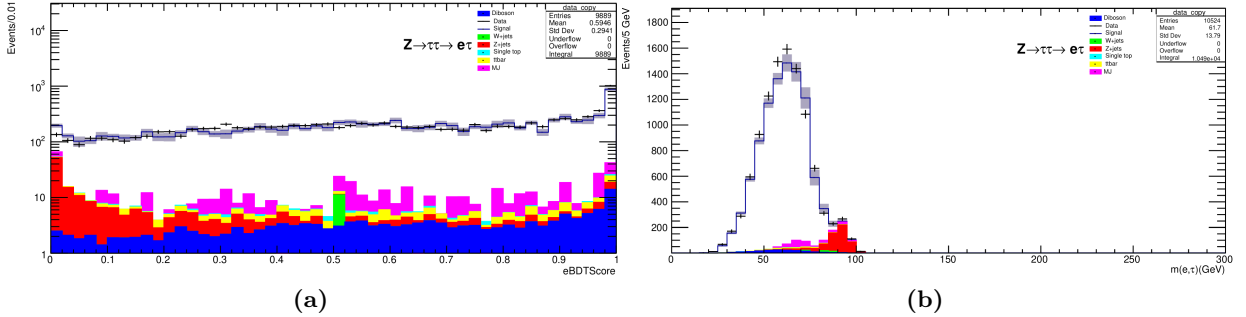


**Figure 11:** Distribution of the variables used for rejecting  $\tau_{\text{had}}$  fakes coming from electrons. On the right  $m(e, \tau_{\text{had}})$  distribution (a) and on the left the eBDTScore distribution (b).

factors on the high- $p_T$  region we select events where  $p_T(\tau_{\text{had}}) \geq 45$  GeV. The  $p_T$  distributions for  $\tau_{\text{had}}$  candidates are shown in Fig.12 for the in between and outside regions.

#### 4.4 Multi Jet Background Estimation

As we said previously,  $\tau_{\text{had}}$  candidates are seeded by jets, thus, QCD events represent a source of background. Nonetheless, we do not have MC simulations for this processes as with the EW

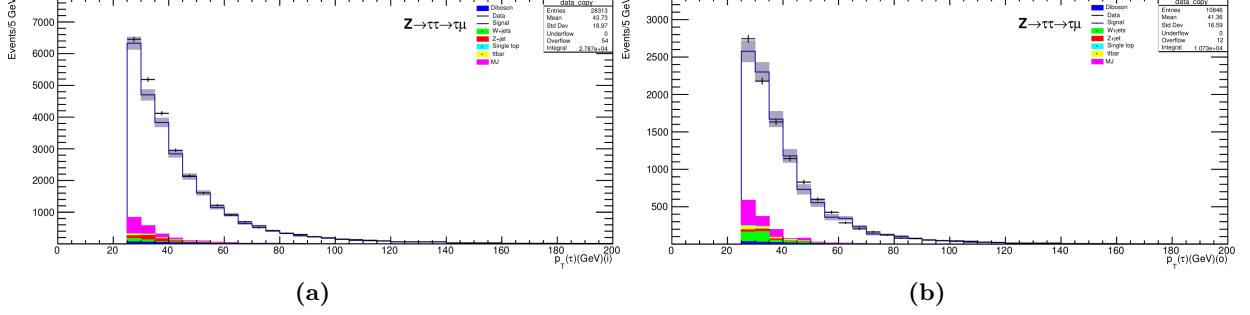


**Figure 12:**  $p_T(\tau_{\text{had}})$  distribution for the in between (a) and outside (b) regions.

interactions shown in Table 3. For this reason, we use a *data driven method* to estimate multi jet (MJ) background. For that purpose, we choose a variable that in principle we suppose is uncorrelated with the shape of the MJ background. For our study, this variable is the relative sign between the charges of the  $\tau_{\text{had}}$  and the lepton. Thus, this defines two regions: the same sign (SS) region where  $q(\tau_{\text{had}}) = q(l)$  and the opposite sign region where  $q(\tau_{\text{had}}) = -q(l)$ . Our estimate of MJ background for the SS region is obtained subtracting signal and electroweak backgrounds (EWBG) simulated contributions, basically:

$$\text{MJBG}_{\text{SS}} = \text{Data}_{\text{SS}} - \text{Signal}_{\text{SS}} - \text{EWBG}_{\text{SS}}, \quad (34)$$

To study the residual charge correlation, we define a control region (CR) where the MJ background is enhanced. This region is defined by events that fail either the lepton isolation criteria or the  $\tau_{\text{had}}$  ID requirement of  $\text{tauRNNScore} > 0.4$  ( $0.55$ ) for 1-prong (3-prong)  $\tau_{\text{had}}$  candidates and have the same other kinematic features of the signal region (SR) described in section 4.3. . A diagram showing the four regions just defined is shown in Fig. . Now if charge correlation is the same in SR and CR, we have:

$$\frac{\text{MJBG}_{\text{SRROS}}}{\text{MJBG}_{\text{SRSS}}} = \frac{\text{MJBG}_{\text{CROS}}}{\text{MJBG}_{\text{CRSS}}}, \quad (35)$$

then,

$$\text{MJBG}_{\text{SRROS}} = \text{MJBG}_{\text{SRSS}} \times \text{RQCD} \quad (36)$$

where  $\text{RQCD} \equiv \frac{\text{MJBG}_{\text{CROS}}}{\text{MJBG}_{\text{CRSS}}}$ .

# 5 Results

The approach usually starts with the problem definition and continues with what you have done. Try to give an intuition first and describe everything with words and then be more formal like ‘Let  $g$  be ...’.

## 5.1 $\mu\tau$ Final state

## 5.2 $e\tau$ Final state

Start with a very short motivation why this is important. Then, as stated above, describe the problem with words before getting formal.

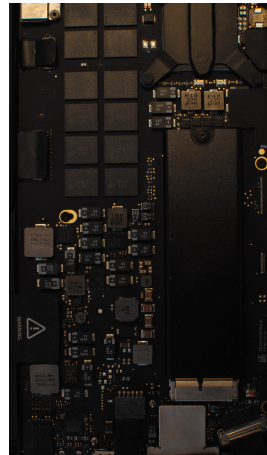
## 5.3 Monte Carlo and data discrepancies



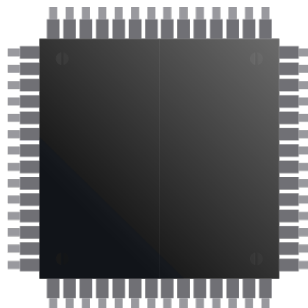
## 6 Conclusions and prospects

Type	Accuracy
A	$82.47 \pm 3.21$
B	$78.47 \pm 2.43$
C	$84.30 \pm 2.35$
D	$86.81 \pm 3.01$

**Table 4:** Table caption. foo bar...



(a) Some cool graphic



(b) Some cool related graphic

**Figure 13:** Caption that appears under the fig Lorem ipsum dolor sit amet, consectetuer adipiscing elit. Ut purus elit, vestibulum ut, placerat ac, adipiscing vitae, felis. Curabitur dictum gravida mauris. Nam arcu libero, nonummy eget, consectetuer id, vulputate a, magna. Donec vehicula augue eu neque. Pellentesque habitant morbi tristique senectus et netus et malesuada fames ac turpis egestas. Mauris ut leo. Cras viverra metus rhoncus sem. Nulla et lectus vestibulum urna fringilla ultrices. Phasellus eu tellus sit amet tortor gravida placerat. Integer sapien est, iaculis in, pretium quis, viverra ac, nunc. Praesent eget sem vel leo ultrices bibendum. Aenean faucibus. Morbi dolor nulla, malesuada eu, pulvinar at, mollis ac, nulla. Curabitur auctor semper nulla. Donec varius orci eget risus. Duis nibh mi, congue eu, accumsan eleifend, sagittis quis, diam. Duis eget orci sit amet orci dignissim rutrum.

# Bibliography

- [1] M. Davier, A. Höcker, and Z. Zhang, “The physics of hadronic tau decays,” *Reviews of Modern Physics*, vol. 78, p. 1043–1109, Oct 2006.
- [2] H. F. A. Group, *Average of  $R(D)$  and  $R(D^*)$  for Spring 2019*, 2019.
- [3] C. Deutsch, B. Martin dit Latour, and C. Grefe, “Identification of hadronic tau lepton decays using neural networks in the ATLAS experiment,” Tech. Rep. ATL-COM-PHYS-2019-773, CERN, Geneva, Jun 2018. RNN tau ID, ATL-PHYS-PUB-2019-033.
- [4] M. L. Perl, G. S. Abrams, A. M. Boyarski, M. Breidenbach, D. D. Briggs, F. Bulos, W. Chinowsky, J. T. Dakin, G. J. Feldman, C. E. Friedberg, D. Fryberger, G. Goldhaber, G. Hanson, F. B. Heile, B. Jean-Marie, J. A. Kadyk, R. R. Larsen, A. M. Litke, D. Lüke, B. A. Lulu, V. Lüth, D. Lyon, C. C. Morehouse, J. M. Paterson, F. M. Pierre, T. P. Pun, P. A. Rapidis, B. Richter, B. Sadoulet, R. F. Schwitters, W. Tanenbaum, G. H. Trilling, F. Vannucci, J. S. Whitaker, F. C. Winkelmann, and J. E. Wiss, “Evidence for anomalous lepton production in  $e^+ - e^-$  annihilation,” *Phys. Rev. Lett.*, vol. 35, pp. 1489–1492, Dec 1975.
- [5] M. Tanabashi, K. Hagiwara, K. Hikasa, K. Nakamura, Y. Sumino, F. Takahashi, J. Tanaka, K. Agashe, G. Aielli, C. Amsler, M. Antonelli, D. M. Asner, H. Baer, S. Banerjee, R. M. Barnett, T. Basaglia, C. W. Bauer, J. J. Beatty, V. I. Belousov, J. Beringer, S. Bethke, A. Bettini, H. Bichsel, O. Biebel, K. M. Black, E. Blucher, O. Buchmuller, V. Burkert, M. A. Bychkov, R. N. Cahn, M. Carena, A. Ceccucci, A. Cerri, D. Chakraborty, M.-C. Chen, R. S. Chivukula, G. Cowan, O. Dahl, G. D’Ambrosio, T. Damour, D. de Florian, A. de Gouvêa, T. DeGrand, P. de Jong, G. Dissertori, B. A. Dobrescu, M. D’Onofrio, M. Doser, M. Drees, H. K. Dreiner, D. A. Dwyer, P. Eerola, S. Eidelman, J. Ellis, J. Erler, V. V. Ezhela, W. Fettscher, B. D. Fields, R. Firestone, B. Foster, A. Freitas, H. Gallagher, L. Garren, H.-J. Gerber, G. Gerbier, T. Gershon, Y. Gershtein, T. Gherghetta, A. A. Godizov, M. Goodman, C. Grab, A. V. Gritsan, C. Grojean, D. E. Groom, M. Grünewald, A. Gurtu, T. Gutsche, H. E. Haber, C. Hanhart, S. Hashimoto, Y. Hayato, K. G. Hayes, A. Hebecker, S. Heinemeyer, B. Heltsley, J. J. Hernández-Rey, J. Hisano, A. Höcker, J. Holder, A. Holtkamp, T. Hyodo, K. D. Irwin, K. F. Johnson, M. Kado, M. Karliner, U. F. Katz, S. R. Klein, E. Klemp, R. V. Kowalewski, F. Krauss, M. Kreps, B. Krusche, Y. V. Kuyanov, Y. Kwon, O. Lahav, J. Laiho, J. Lesgourgues, A. Liddle, Z. Ligeti, C.-J. Lin, C. Lippmann, T. M. Liss, L. Littenberg, K. S. Lugovsky, S. B. Lugovsky, A. Lusiani, Y. Makida, F. Maltoni, T. Mannel, A. V. Manohar, W. J. Marciano, A. D. Martin, A. Masoni, J. Matthews, U.-G. Meißner, D. Milstead, R. E. Mitchell, K. Mönig, P. Molaro, F. Moortgat, M. Moskovic, H. Murayama, M. Narain, P. Nason,

- S. Navas, M. Neubert, P. Nevski, Y. Nir, K. A. Olive, S. Pagan Griso, J. Parsons, C. Patrignani, J. A. Peacock, M. Pennington, S. T. Petcov, V. A. Petrov, E. Pianori, A. Piepke, A. Pomarol, A. Quadt, J. Rademacker, G. Raffelt, B. N. Ratcliff, P. Richardson, A. Ringwald, S. Roesler, S. Rolli, A. Romanouk, L. J. Rosenberg, J. L. Rosner, G. Rybka, R. A. Ryutin, C. T. Sachrajda, Y. Sakai, G. P. Salam, S. Sarkar, F. Sauli, O. Schneider, K. Scholberg, A. J. Schwartz, D. Scott, V. Sharma, S. R. Sharpe, T. Shutt, M. Silari, T. Sjöstrand, P. Skands, T. Skwarnicki, J. G. Smith, G. F. Smoot, S. Spanier, H. Spieler, C. Spiering, A. Stahl, S. L. Stone, T. Sumiyoshi, M. J. Syphers, K. Terashi, J. Terning, U. Thoma, R. S. Thorne, L. Tiator, M. Titov, N. P. Tkachenko, N. A. Törnqvist, D. R. Tovey, G. Valencia, R. Van de Water, N. Varelas, G. Venanzoni, L. Verde, M. G. Vincter, P. Vogel, A. Vogt, S. P. Wakely, W. Walkowiak, C. W. Walter, D. Wands, D. R. Ward, M. O. Wascko, G. Weiglein, D. H. Weinberg, E. J. Weinberg, M. White, L. R. Wiencke, S. Willocq, C. G. Wohl, J. Womersley, C. L. Woody, R. L. Workman, W.-M. Yao, G. P. Zeller, O. V. Zenin, R.-Y. Zhu, S.-L. Zhu, F. Zimmermann, P. A. Zyla, J. Anderson, L. Fuller, V. S. Lugovsky, and P. Schaffner, “Review of particle physics,” *Phys. Rev. D*, vol. 98, p. 030001, Aug 2018.
- [6] E. Fermi, “Tentativo di una teoria dei raggi beta,” *Il Nuovo Cimento (1924-1942)*, vol. 11, no. 1, pp. 669–688, 1932.
  - [7] S. Schael *et al.*, “Precision electroweak measurements on the  $Z$  resonance,” *Phys. Rept.*, vol. 427, pp. 257–454, 2006.
  - [8] A. Pich, “Precision Tau Physics,” *Prog. Part. Nucl. Phys.*, vol. 75, pp. 41–85, 2014.
  - [9] S. Schael *et al.*, “Electroweak Measurements in Electron-Positron Collisions at W-Boson-Pair Energies at LEP,” *Phys. Rept.*, vol. 532, pp. 119–244, 2013.
  - [10] G. Ciezarek, M. Franco Sevilla, B. Hamilton, R. Kowalewski, T. Kuhr, V. Lüth, and Y. Sato, “A challenge to lepton universality in b-meson decays,” *Nature*, vol. 546, p. 227–233, Jun 2017.
  - [11] A. Airapetian *et al.*, “ATLAS: Detector and physics performance technical design report. Volume 1,” 5 1999.
  - [12] G. Aad *et al.*, “Identification and energy calibration of hadronically decaying tau leptons with the ATLAS experiment in  $pp$  collisions at  $\sqrt{s}=8$  TeV,” *Eur. Phys. J. C*, vol. 75, no. 7, p. 303, 2015.
  - [13] M. Cacciari, G. P. Salam, and G. Soyez, “The anti- $k_t$  jet clustering algorithm,” *JHEP*, vol. 04, p. 063, 2008.
  - [14] G. Aad *et al.*, “Topological cell clustering in the ATLAS calorimeters and its performance in LHC Run 1,” *Eur. Phys. J. C*, vol. 77, p. 490, 2017.

